Understanding the effect of cycling lithium-ion pouch cells under stress using neutron diffraction

Juliane I. Preimesberger [a], Yan Chen [b], Ke An [b], Craig B. Arnold [a],[*]

[a] *Department Mechanical and Aerospace Engineering, Princeton University, Princeton, NJ, 08544, USA*
[b] *Neutron Scattering Division, Oak Ridge National Laboratory, Oak Ridge, TN, 37831, USA*

HIGHLIGHTS

- Neutron diffraction reveals how stack pressure affects charging lithium-ion cells.
- Lithium-ion pouch cells lose capacity when charged under applied stress.
- Copper current collector experiences significant strain during charge cycling.
- Electrode phase transitions require more charge under higher stack pressures.

ARTICLE INFO

ABSTRACT

Large volume changes of lithium-ion batteries during battery operation affect battery lifetime and performance through mechanical degradation. Therefore, understanding the coupling between mechanics and electrochemistry in these systems is crucial. In this work, we use neutron diffraction to learn how commercial lithium-ion pouch cells are affected by stack pressure during charge and discharge. We find that a change in stack pressure affects the phase transitions in electrode materials, requiring more charge to reach higher state-of-charge phases which results in effective capacity loss for the battery. Also noteworthy is that the copper current collector experiences strain during charge and discharge due to the expansion of the graphite anode, something often overlooked in these systems.

1. Introduction

It is widely recognized that mechanics and electrochemistry are fundamentally linked in lithium-ion batteries [1–6]. During charge and discharge, many lithium-ion electrodes experience significant volume changes that affect the structural integrity of battery components by causing wear-and-tear on crucial interfaces [5–8]. Consequently, a multitude of studies have investigated this mechano-electrochemical coupling in lithium-ion systems, usually focusing on freely expanding systems [9–18]. However, mechanical degradation due to electrode volume change is particularly important for batteries operating in constrained spaces (such as battery packs) and under stack pressures (such as solid-state systems) [7,19,20]. Therefore, it is essential to examine this mechano-electrochemical coupling in systems under external stress.

While there are many in-situ techniques employed to investigate the mechanics and electrochemistry of lithium-ion batteries, neutron scattering measurements are particularly effective. This is because the nonlinear neutron cross section allows for the study of lighter elements (such as carbon) commonly found in anodes, and the long penetration distances and large beam size permit bulk sample measurements that eliminate complicated sample preparation [15–17,21,22]. Accordingly, a number of neutron scattering studies have been used to look at lithium-ion batteries, including the mechano-electrochemical coupling of the electrodes [15–18]. In particular, neutron diffraction of pouch cells provides insight into the crystallographic phase and lattice changes due to lithium insertion or de-insertion [17,23–25].

In lithium-ion electrodes, the electrochemical potential of the lithium ions changes with stress; in a material that expands with lithium insertion (such as graphite), an applied stress forces the lattice to compress, which makes it thermodynamically favorable for some of the ions to leave the lattice structure to comply with the lattice strain [26–30]. If ions cannot leave the structure, the cell potential is raised;

thus, if the cell was being charged under stress (where the charging current is assumed to be much higher than the current generated from the mechano-electrochemical coupling) the cell potential is slightly higher than without stress. This is particularly critical for large-volume expansion electrodes, such as silicon or sulfur electrodes, as this change in electrochemical potential is large. However, this effect is still present in graphite and lithium cobalt oxide commercial cells, which are more convenient to study as they have consistent quality across cells.

This mechano-electrochemical effect is expected to affect the phase transitions that occur in electrode materials. To investigate this, neutron diffraction charge-cycling experiments were conducted on commercial pouch cells under constant applied stress. It was found that an increase of stack stress changes the required amount of charge required for phase transitions for graphite and lithium-cobalt oxide electrodes, and thus this increase causes a small amount of capacity loss. Additionally, it was found there is strain in the copper foil that is correlated with the expansion of the graphite anode during charge and discharge. These findings have important implications for understanding mechanical degradation in lithium-ion systems under stress.

2. Experimental

In-situ neutron diffraction measurements were conducted at VULCAN, a state-of-the-art time-of-flight neutron diffractometer at the Spallation Neutron Source (SNS) at Oak Ridge National Laboratory [21, 22]. For this experiment, commercial lithium-ion 500-mAh jelly-rolled (wound 17 times) pouch cells (GMB Power® 652535), with a graphite anode, porous polymer separator, and lithium cobalt oxide (LCO) cathode, were used. The pouch cell was placed in the VULCAN MTS® load frame at a 45° to the incident beam, as was done in previous work [31]. The neutron beam was positioned in the middle of the cell (full cell volume was $23.5 \times 30 \times 6.5$ mm^3 and the neutron beam gauge volume was $5 \times 12 \times 5$ mm^3, determined by the beam incident slits and receiving collimators). Aluminum plates were used as spacers for the pouch cell, to limit the interaction of the load frame with the neutron beam. However, the gauge volume of the beam still contained some of the aluminum spacers so the resulting data had strong aluminum peaks. The high-intensity configuration and the 30 Hz chopper frequency was used, and the time-of-flight neutron events were continuously collected during the in-situ measurements.

Different constant loads of 0, -10, and -20 MPa (which corresponds to 0, -7 and -14 kN of compressive force over the entire pouch) were placed on the cell for the duration of the experiment. The maximum stress placed on these cells is limited primarily by the polymer separator, which experiences pore closure above 25 MPa stack pressure [31,32]. To load the cell to the selected stress prior to neutron diffraction, a loading rate of 0.33 MPa s^{-1} was used. A Biologic® SP-300 potentiostat was used to charge and discharge the cell. An initial equilibration period of around 100 min allows the polymer components of the cell to viscoelastically deform and reach a quasi-steady-state mechanical equilibrium. Then, the cell was fully discharged at 100 mA to 2.75 V. Next, the cell was charged at 100 mA, or a rate of C/5, to 4.2 V. Finally, a full discharge step at 100 mA to 2.75 V was performed.

The neutron events were sliced and binned into histograms corresponding to a change of 1 % state-of-charge (approximately 3 min) using VDRIVE software [33]. Single peak fitting for each histogram was performed using Matlab's least squares fitting function. The pseudo-Voight peak profile function was used, as a reasonable simplification, to fit the *in-situ* diffraction peaks that do not appear significantly asymmetric, though it is known that a more complicated back-to-back exponential convoluted pseudo-Voight peak shape best represents the time-of-flight neutron diffraction pattern [34]. A local linear background was subtracted for each peak prior to fitting.

3. Results and discussion

In lithium-ion batteries, which are considered mechano-electrochemical systems, cell potential shifts higher under stack pressure during charge [26–30]. Both the graphite and LCO electrodes in the pouch cells used in this study are expanding during charge, with graphite expanding due to lithium insertion and LCO expanding due to lithium extraction [35,36]. Thus, compressing the electrode lattices makes it electrochemically favorable for a small amount of lithium to leave the graphite lattice and enter the LCO lattice to reduce the lattice strain. However, the charging current is forcing the lithium ions to move in the opposite direction (from LCO to graphite) and is orders of magnitude higher than the mechano-electrochemical current (100 mA at C/5 compared to 1 mA) [28–30]. Therefore, the lithium ions cannot relax the mechano-electrochemical strain, so the cell potential is raised. During discharge, an applied stress still makes it favorable for lithium to move from graphite to LCO, which is the same direction as the discharge current, resulting in a faster discharge which effectively lowers the cell potential.

Fig. 1a plots the charge and discharge curves at room temperature and a C/5 rate (100 mA) with respect to time at different stress levels. As expected, under stress, the potential of the cell is higher during charge and lower during discharge. As the pouch cells are charge-cycled with a constant current scheme, these shifts in potentials result in a faster charge and discharge step for higher stresses, at the cost of capacity. The capacities of each charge and discharge step are reported in Fig. 1a, and the nominal capacity of these cells is 500 mA h, as stated by the manufacturer, though cells typically have slightly higher actual capacity at 510 mA h. Although there is slight capacity variation among these commercial cells (around 10 mA h variation between cells), the difference in capacity due to stress, particularly for 20 MPa, indicates that under a constant current charging scheme, some capacity is lost. This loss of capacity is due in large part to the voltage cutoffs (4.2 V for charging and 2.75 V for discharging) being reached earlier when the cell is under stress, and without a constant voltage (CV) step this capacity is not recovered. This indicates that if a lithium-ion system is known to be under stress during its operation, the cutoff voltage window might need to be adjusted to extract the full capacity if no CV step is used. Losses in capacity might be due to differences in cell impedances, which increase under applied stress. Additional contributions to the higher-stress capacity losses might be related to compression of the electrode microstructure (such as the closing of pores).

The state-of-charge (SOC) is defined using the capacities listed in Fig. 1a, where the end is 100 % relative SOC (where SOC is calculated using the capacity of the charge or discharge step). Fig. 1b plots the differential capacity (dQ/dV) of the cells versus SOC. The differential capacity is often used to understand the electrochemical reactions happening within the cell, as the peaks in a dQ/dV charging curve roughly correspond to electrode phase transitions [35–37]. As stress increases, the charging and discharging dQ/dV peaks shift, indicating that the cell overpotentials are increasing and electrode phase transitions are shifting to different SOCs under higher stresses. This shift in SOC might also contribute to the capacity loss under stress. To investigate this, neutron diffraction can be used to identify the SOC at which phase transitions occur at a given stress.

Fig. 2 shows the neutron diffraction results at 0 MPa for cycling at C/5. In Fig. 2a, the center shows the diffraction results for a range of d-spacings (1.65–2.45 Å), binned into 1 % SOC histograms (about 3 min). Intensities outside of the arbitrary range are shown in white. Diffraction peaks are identified for this range of d-spacings for graphite and LCO electrode, and copper and aluminum current collector, phases [17,23, 24]. Graphite phases are labeled following the conventions from Ref. [23], where stage 1 L has the structure of graphite, stage 4 L has ABAB stacking with a few lithium ions in between the layers, stage 3 L is LiC$_{30}$, stage 2 L is LiC$_{18}$, stage 2 is LiC$_{12}$, and stage 1 is LiC$_6$. On the left of Fig. 2a, the applied current during a C/5 charge and discharge cycle is
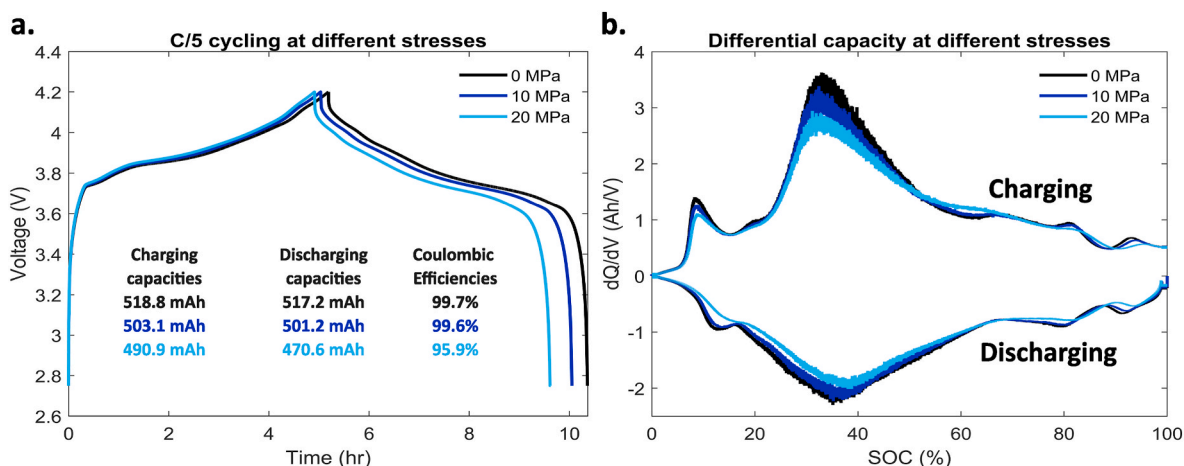
Fig. 1. Effect of stress on pouch cell charge and discharge curves
(a) C/5 charging and discharging curves for LCO/graphite pouch cells under different stress levels versus time, with capacities of each step reported. (b) The differential capacity (dQ/dV) of the cell versus SOC.
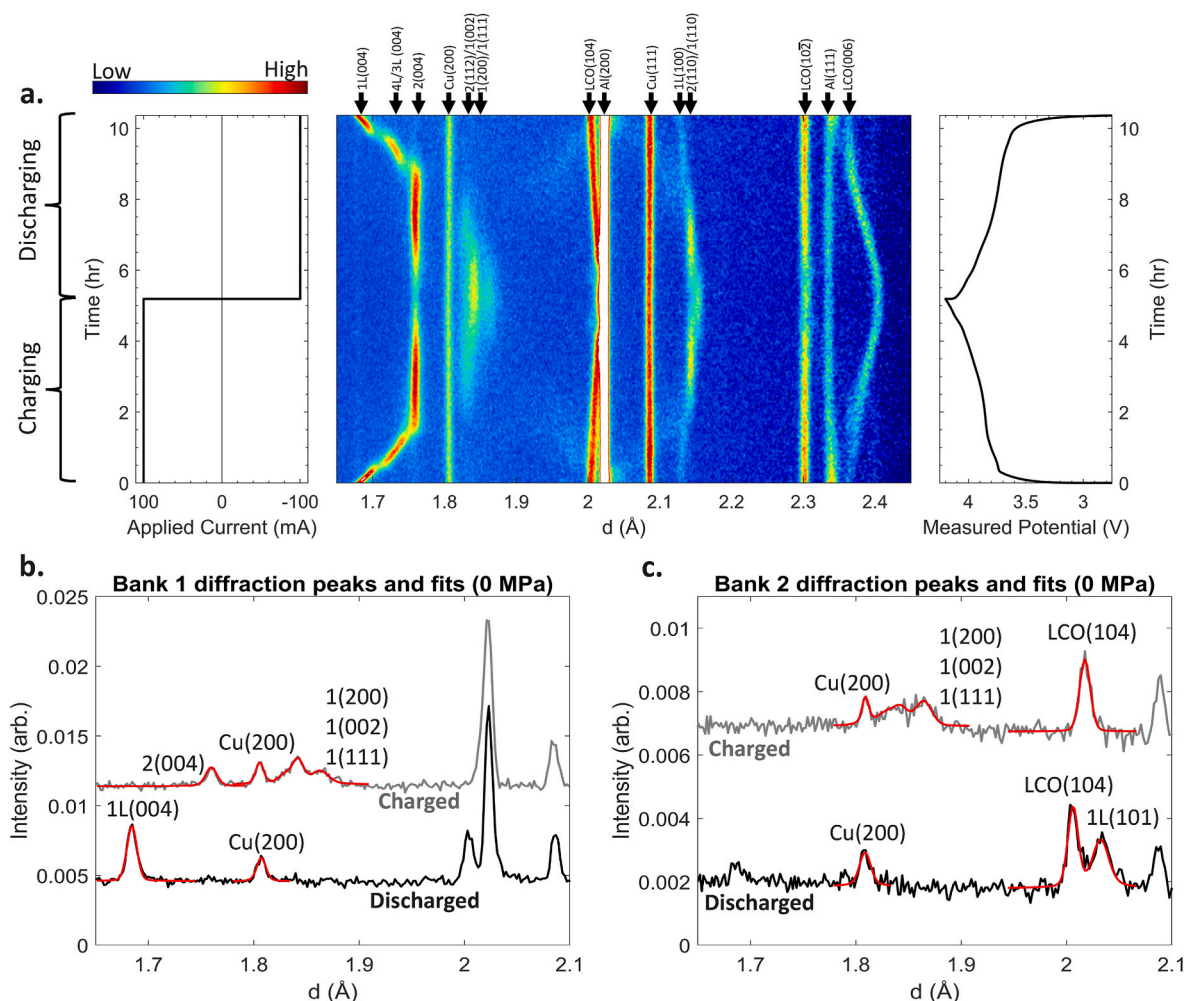

Fig. 2. Pouch cell diffraction results during C/5 cycling for 0 MPa
(a) (Left) Applied current of the pouch cell during C/5 cycling. (Center) Diffraction patterns at 0 MPa, with patterns binned into 1 % SOC histograms. Peaks are identified. Intensities outside of the arbitrary range (0.0033–0.0085) are shown in white. (Right) The measured voltage of the pouch cell during C/5 cycling, at 0 MPa. (b) The Bank 1 (grains aligned with loading direction) diffraction pattern of the cell at 0 MPa at full charge and discharge, and corresponding fits of important peaks. (c) The Bank 2 (grains perpendicular to loading direction) diffraction pattern of the cell at 0 MPa at full charge and discharge, and corresponding fits of important peaks.

plotted, and on the right, the measured voltage of the cell under 0 MPa is plotted.

From Fig. 2a, it can be seen that the lithiated graphite anode (004) and (110) peaks change drastically in d-spacing during charging and discharging, while the copper current collector (200) and (111) peaks vary little with SOC, which is consistent with previous experimental results of lithium-ion electrode expansion [17,23,25,38]. Additionally, higher lithiated graphite phases (stages 1 and 2) have peaks that only show up once the cell has reached sufficient charge (such as the peaks around 1.85 Å), also consistent with previous results [17,23,25,38]. As expected, the LCO (104) and LCO (006) cathode peaks also change with SOC, though the LCO (10$\bar{2}$) does not, likely because it is not orthogonal to the c-axis, where the most expansion takes place [24,35].

Diffraction patterns at all stress levels are plotted in Fig. S2. To determine the structural evolution of the pouch cell materials, the positions of each peak are tracked through single peak fitting. Single peak fitting for each histogram and stress was performed for the copper (200), lithiated graphite (004), and LCO (104) peaks. These peaks were selected because they had a strong signal and limited overlap between other peaks. The LCO (104) peak was taken from the +90° detector data (called Bank 2), which captures the diffraction peaks for the grains perpendicular to the loading direction (Fig. 2a shows the −90° detector data, called Bank 1, or grains aligned with the loading direction). Due to grain texture, the aluminum (200) peak is much weaker perpendicular to the loading direction, so the LCO (104) peak is visible throughout all SOCs. For fitting LCO (104), the Al (200) peak was subtracted out from the diffraction patterns as it was constant throughout cycling (see Fig. S4). Due to the beam spacer, the aluminum current collector peaks and aluminum spacer peaks cannot be distinguished, so no aluminum phase peaks were fitted. The diffraction patterns for the cell at 0 MPa at full charge and discharge for Bank 1 are plotted in Fig. 2b, with single peak fits plotted. As copper (200) is near lithiated graphite peaks 1 (200), 1 (111), 1 (002) at full charge, all were fitted together to ensure accurate results for the copper peak at high SOCs. The diffraction patterns and single peak fits for Bank 2 (with Al (200) subtracted) are

shown in Fig. 2c. At low SOCs, the graphite 1 L (101) peak is near the LCO (104) peak, so both peaks were fit to make sure the LCO (104) results were accurate.

First, we look at the single peak fit results from the copper (200) peak. Fig. 3a shows the diffraction pattern around the copper (200) peak for the 0 MPa experiment, with nearby peaks identified from graphite stages 1 and 2. Fig. 3b plots the fitted d-spacings of the copper (200) peak during charge and discharge against SOC during the 1 % SOC time slice for each stress level. As expected, a higher stress results in a smaller d-spacing for copper (200), indicating that the lattice is being compressed, though the magnitude of this stress is higher than expected at 0 % SOC. While the peak fits do have large error bars due to the operando data collection (each slice is averaged over 1 % SOC of the battery), the trend between stress levels is clear. We can calculate the (200) lattice strain from Fig. 3b for each stress at 0 % SOC using Equation (1), where $d_{0,y}$ is the d-spacing at a given stress (−10, −20 MPa), where SOC is set to 0 %, $d_{0,0}$ is the d-spacing at 0 MPa and 0 % SOC, and $\varepsilon_{0,MPa}$ is the strain at 0 % SOC at a given stress level, in the normal (along loading direction, denoted by superscript *N*) or in-plane (transverse to loading direction, denoted by superscript *P*) directions:

$$\varepsilon_{0,MPa} = \frac{d_{0,MPa} - d_{0,0}}{d_{0,0}} \qquad (1)$$

For −10 and −20 MPa, the strains for Bank 1 (normal to cell) at 0 % SOC are $\varepsilon_{0,-10}^{N} = -8 \times 10^{-4}$ and $\varepsilon_{0,-20}^{N} = -1.3 \times 10^{-3}$, with the standard error for the peak fitting approximately 2.8×10^{-4} for both. We can also fit the copper (200) peak from Bank 2 data (along the plane of the cell); see Fig. S3 for fit results. The in-plane strains for copper (200) are $\varepsilon_{0,-10}^{P} = 3.9 \times 10^{-4}$ and $\varepsilon_{0,-20}^{P} = 7 \times 10^{-4}$, with the standard error of around 4.8×10^{-4} for both. Along the (100) lattice plane, the diffraction elastic modulus of copper is 101.1 GPa and the Poisson's ratio is 0.38 [39]. Using 3D Hooke's law, and assuming that the two in-plane dimensions of the pouch cell are approximately the same, we can estimate the normal and in-plane stresses on the pouch cell to calculate the
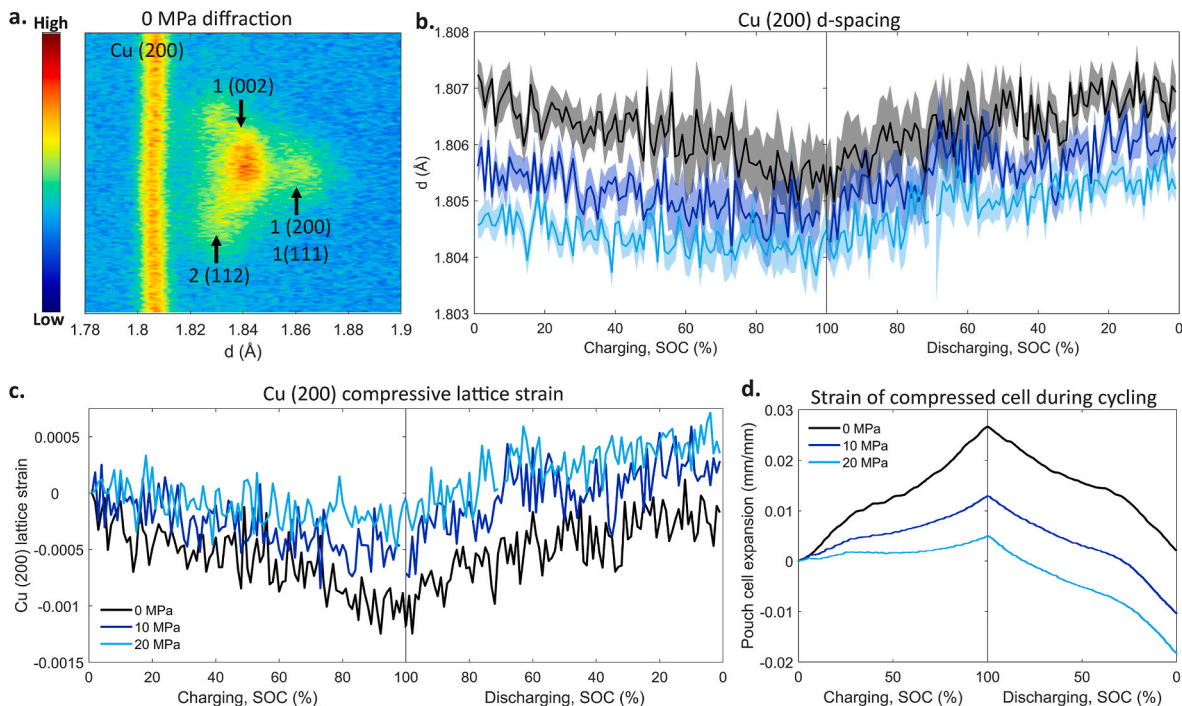

Fig. 3. Copper peak spacings at different stress levels. (a) The diffraction pattern around the copper (200) peak (zoomed-in from Fig. 2); arbitrary intensities range from 0.003 to 0.0075. (b) Fitted d-spacings at different stress levels; the shaded regions represent the standard error from the fit results. (c) Compressive lattice strain for Cu (200), with respect to the copper d-spacing at 0 MPa and 0 % SOC. (d) Expansion of each pouch cell during cycling, normalized by pouch cell thickness (6.5 mm).

deviatoric stresses in the normal direction ($\sigma_{D,N}$), reported in Table 1. We choose to look at deviatoric stresses because this reduces the error due to fitting by eliminating uncertainties about the $d_{0,0}$ position [40]. Although the change of normal deviatoric stress $\sigma_{D,N}$ is higher than the nominal applied stress of −10 and −20 MPa calculated based on contact area of the compression platens, given the uncertainties in the copper peak position (estimated deviatoric stress error is reported in Table 1), this is not unreasonable. Additional contributions to this discrepancy could be stress concentrations within the pouch cell or the anisotropy and texture of the copper foil.

From Fig. 3b it is clear there is a slight dependence on SOC for all stress levels, where at higher SOCs, the copper lattice is compressed (indicated by the decreasing d-spacing towards 100 % SOC). In the literature, there are reports that show a difference in tensile strain for copper current collectors connected to lithiated graphite (after the graphite was lithiated to a given SOC, it was then scraped off and the copper was measured by itself) [41]. However, it seems unlikely that the copper is electrochemically active (lithium preferentially plates on copper instead of lithiating copper). A more likely explanation of this effect of SOC is that the graphite anode material is expanding during charge and therefore creating internal stresses in the pouch cell which strain the copper current collector. Fig. 3a shows that the appearance of the graphite stage 1 and 2 peaks roughly correlate to where the (200) peak decreases slightly, supporting this possibility. Another contribution to the change in copper lattice might be due to thermal expansion during charge cycling, caused by Joule heating due to internal resistances [42].

Fig. 3c plots the lattice strain of the (200) peak, calculated using Equation (2), where $d_{0,MPa}$ is the d-spacing at the given stress level at 0 % SOC , $d_{x,MPa}$ is the d-spacing at the given stress level at a given SOC (x), and $\varepsilon_{x,MPa}$ is the normal or in-plane strain at a given stress level and SOC. The difference between strain in the charging and discharging step could be due to the viscoelastic creep of polymeric materials in the pouch cell affecting the actual stress on the copper over time. This is supported by the plot of each cell's expansion during charge and discharge, shown in Fig. 3d, normalized by the cell thickness of 6.5 mm to get strain. The pouch cell expansion for −10 and −20 MPa does not return to zero after the discharge step, indicating that there was still significant creep happening during the charging step, despite the 100-min waiting period before the start of the experiment. While during the charging step the strain is less for higher stresses, the difference in total pouch cell strain during the entire discharge step is approximately the same for each stress (∼ 0.024 mm/mm). Similarly, from Fig. 3c, while the lattice strain of copper (200) is different during charging, the total strain during the full discharge step is similar for all three stress levels in the normal direction.

$$\varepsilon_{x,MPa} = \frac{d_{x,MPa} - d_{0,MPa}}{d_{0,MPa}} \tag{2}$$

As before, we can use 3D Hooke's law to estimate stresses due to charge cycling a pouch cell; Table 2 reports the strain of d-spacings at 100 % SOC versus 0 % SOC (at the discharge step) in the normal and in-plane directions ($\varepsilon_{100,MPa}^{N}$ and $\varepsilon_{100,MPa}^{P}$) as well as the normal deviatoric stresses. The change in normal deviatoric stress due to charge cycling is similar for all stress levels, given the estimated error. As discussed earlier, uncertainties in the strain calculation and the complex stress environment in the pouch cell make it difficult to directly compare the nominal stress with the calculated copper (200) strain. Also, it is possible some of this strain is

Table 1
Estimated stresses of the copper (200) peak at 0 % SOC from 3D Hooke's law.

Applied Stress (MPa)	$\sigma_{D,N}$ (MPa)
0	0
−10	−58 ± 16
−20	−98 ± 17

Table 2
Estimated stresses of the copper (200) peak due to charge and discharge.

Applied Stress (MPa)	$\varepsilon_{100,MPa}^{N}$ (Å/Å)	$\varepsilon_{100,MPa}^{P}$ (Å/Å)	$\sigma_{D,N}$ (MPa)
0	− 8.4 × 10⁻⁴	3.2 × 10⁻⁴	−56 ± 35
−10	− 8.3 × 10⁻⁴	8.1 × 10⁻⁴	−81 ±27
−20	− 7.0 × 10⁻⁴	9.2 × 10⁻⁴	−79 ±25

due to thermal expansion, which should approximately be the same for all cells as the internal resistances of the cells should be similar, with a slight increase under stack pressure [42]. However, we expect the contribution of thermal expansion to be very small as we are operating at slow rate (0.2C) and the cells we are testing are not large-format. Regardless, while the stresses due to charge cycling calculated for these commercial cells is not high enough to plastically deform the copper foil, electrodes with larger volume expansions, like silicon, experience mechanical degradation of the current collector [43]. This suggests that the significant internal stress on the copper foil that results from the expansion of the anode during charge and discharge should not be neglected in discussions on mechanical studies of these electrodes.

Next, we turn to understanding what happens to the electrode structures during cycling under stress. Fig. 4a shows the diffraction pattern of the LCO (104) peak at 0 MPa, from the Bank 2 detector, with Al (200) subtracted. At 0 % SOC, LCO starts out as a rhombohedral lattice (labeled R) which has a strong (104) peak, that increases in d-spacing as SOC increases, as expected due to the c-axis expansion due to lithium extraction [24,35]. In the region of 80–100 % SOC, the (104) peak splits into two peaks; one stronger peak at around 2.02 Å, and a weaker peak at 2.004 Å. This behavior agrees well with the transition in LCO from the rhombohedral lattice to the monoclinic lattice which was reported in the literature [24,35,44]. Therefore, we use the notation of the monoclinic phase by labeling the peak at 2.02 Å as M (111) and the peak at 2.004 Å as M (20$\bar{2}$) [44]. As can be seen from the discontinuities of the (104) peak in Fig. 4a, this phase transition is reversible during electrochemical cycling: first at around 80 % SOC the rhombohedral lattice transitions to monoclinic, and then the monoclinic lattice transitions back to rhombohedral at around 90 % SOC. Nevertheless, it is noted that the presence of this monoclinic structure is not typically found in commercial LCO cells, but could be attributed to heterogenous lithiation through the cell or other degradation mechanisms [44]. In this region of d-spacings there is also a graphite anode phase 1 L (101) peak (see Fig. S5 for the d-spacings for these peaks).

Fig. 4b plots the fitted d-spacings of the LCO peaks for each stress level. As expected, a higher stress results in a smaller d-spacing, due to mechanical strain. Around 95–100 % SOC, the −20 MPa case has a higher d-spacing, likely because at this stress, the M phase does not fully disappear. At higher stresses, the peak d-spacing switches from the R phase to the M phase (and back) at higher SOCs. This means during both charge and discharge, the phase transitions R ↔ M and M ↔ R happen at higher SOCs with increasing stress. A higher SOC means that the phase transition requires more of the available charge. This is consistent with our expectations; since LCO gains lithium as it contracts, compressing the pouch impedes lithium from leaving the LCO electrode, requiring more of the lithium inventory to leave the structure for the phase transitions to occur.

Graphite, on the other hand, is losing lithium as it contracts, so compressing the pouch cell means some lithium leaves the graphite electrode. Therefore, it can be assumed that graphite phase transitions require more of the lithium inventory to enter the structure to occur. So, it is expected to see the same trend in phase transition SOC as LCO: at higher stresses, transitions require more of the available charge, or a higher SOC. To analyze this, the (004) lithiated graphite peak was analyzed with single peak fitting. Fig. 5a shows the diffraction pattern at 0 MPa for this (004) peak and shows that this peak is not continuous but rather has distinct regions as SOC changes, corresponding to the
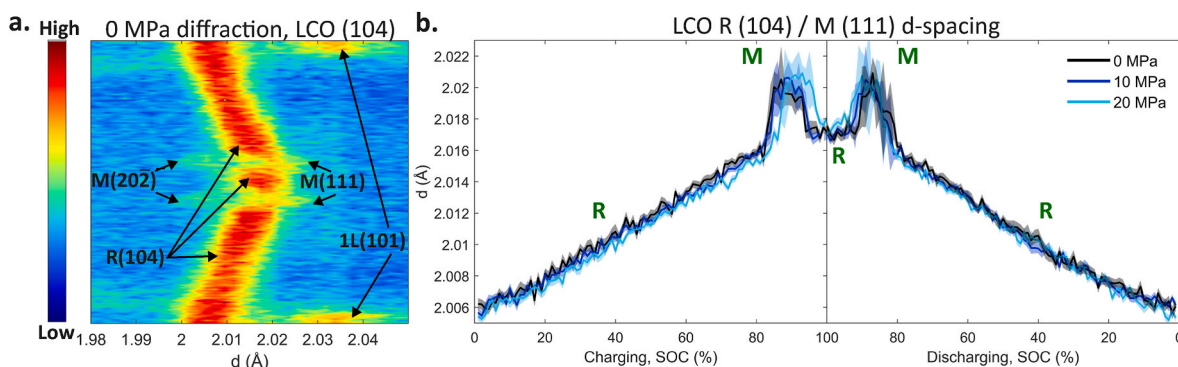
Fig. 4. Diffraction patterns and peak fittings for LCO (104) during charging and discharging. (a) Diffraction pattern of the LCO (104) peak; note that this is from the +90° detector. Arbitrary intensities range from 0.002 to 0.0068. (b) Fitted d-spacings at each stress level for LCO (104). Shaded regions indicate the standard error for the peak fittings, and different phases (R or M) are labeled.
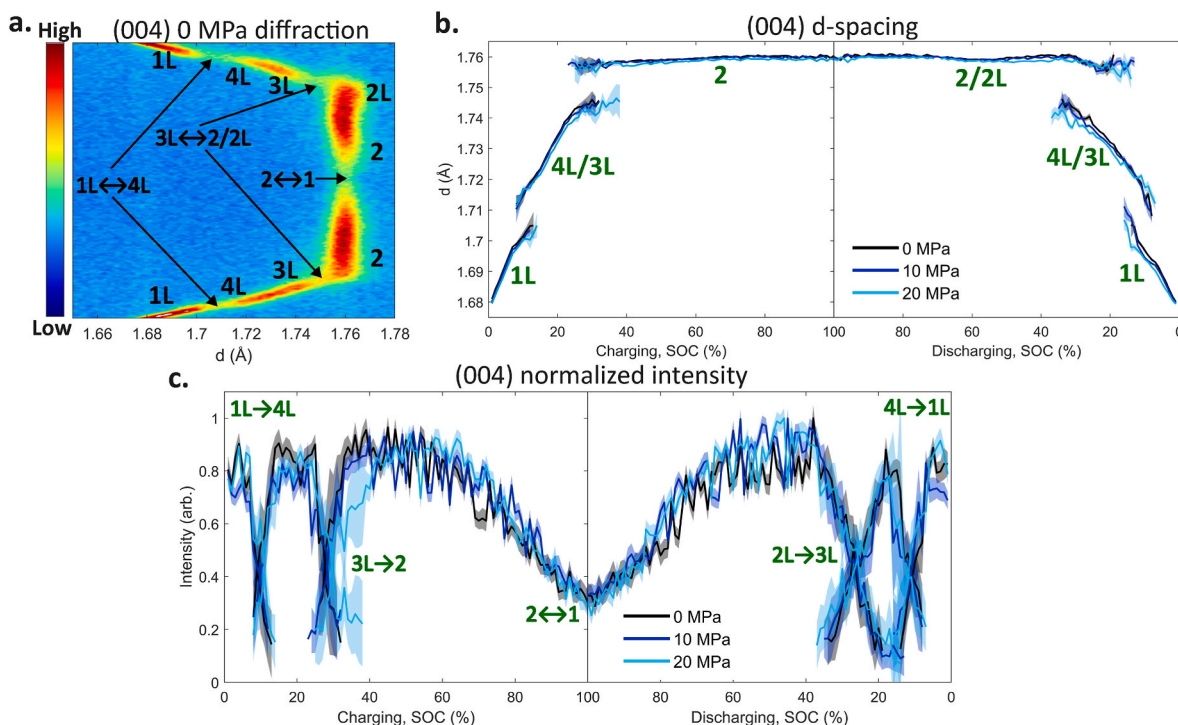

Fig. 5. Lithiated graphite (004) d-spacings at different stress levels
(a) Diffraction pattern for (004) at 0 MPa, with phases and phase transitions identified. Arbitrary intensities range from 0.0027 to 0.0085. (b) The peak spacings for the (004) peak, where shaded regions represent the standard error of the fit, and phases are labeled. (c) Normalized peak intensities, with first-order phase transitions labeled.

presence of different lithiated graphite phases. These phases are labeled in Fig. 5a according to previous literature [23]. First-order phase transitions, which are indicated by local minimums in intensity, are labeled.

As expected for this peak, Fig. 5b shows the peak d-spacing changes drastically with SOC for all stress levels [17,23]. Also, across all SOCs, there is a decrease in d-spacing with stress due to the mechanical deformation of the materials. To clearly see where the phase transition occurs, Fig. 5c plots the normalized peak intensities for each stress level. The expected shift in transition SOC is clear, where the intersection of the two phases' intensities shifts to higher SOC at higher stresses. There is also a similar shift in the intensity decrease around 70 % SOC correlating to the 2 ↔ 1 phase transition. The 4L ↔ 3L transitions for both charge and discharge and the 2→2L transition during discharge are second-order transitions that we are unable to resolve with our peak fitting results. Regardless, the 1L ↔ 4L, 3L ↔ 2/2L, and 2 ↔ 1 transitions show the same trend as LCO: a higher stress leads to a higher phase

transition SOC, therefore requiring more lithium inventory in the graphite for transitions to occur.

From our fits of the LCO and graphite peaks, the SOC at which each phase transition occurs for each stress level can be determined. For the graphite first-order phase transitions, the crossover point in intensity of the (004) peak between two co-existing phases was found using linear fits. Fig. 6a–d shows the linear fits for the 1L ↔ 4L and 3L ↔ 2/2L transitions, where the intersection of the lines shifts to higher SOC at higher stresses. Notably, the 2L→3L transition during discharge, shown in Fig. 6d–is shifted less than the 3L→2 transition during charge in Fig. 6c, suggesting that the 2 L–3 L phase transition is less affected by applied stress than the 3 L to 2 phase transition [23]. The graphite 2 ↔ 1 phase transition is a two-phase region, indicated as the dip in intensity in the (004) peak around 70–100 % SOC. The SOCs for this transition were fit using a Gaussian peak to 1-intensity, as shown in Fig. 6e. The SOC at charge and discharge was defined as the peak center minus three times
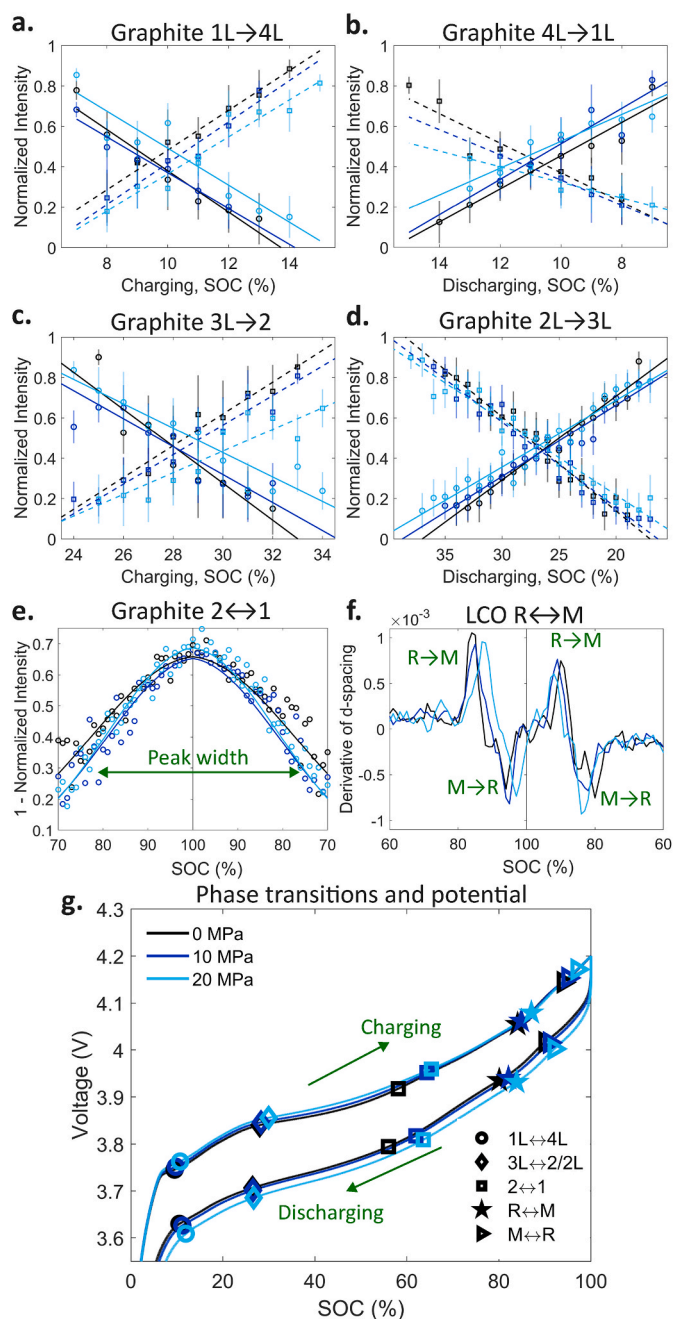
Fig. 6. Voltage and SOCs of the phase transitions at each stress. (a) The 1L→ 4L phase transition with linear fits. (b) The 4L→1L phase transition with linear fits. (c) The 3L→2 phase transition with linear fits. (d) The 2L→ 3L phase transition with linear fits. (e) The 2↔1 phase transition, with a Gaussian fit to 1-intensity of the (004) peak. SOCs of the transition were defined as $\mu - 3\sigma$, where μ is the peak center and σ is the standard deviation. (f) LCO phase transitions between R and M phases, determined from the derivative of d-spacing with respect to SOC. The local minima and maxima indicate the SOC of the transitions. (g) The charge and discharge curves for each stress, with the SOC and cell potential of each phase transition identified.

the standard deviation σ, which covers 99.7 % of the peak width. For the LCO transitions, the derivative of the d-spacing of the R (104) and M (111) peaks with respect to stress was taken, and local minima and maxima of this derivative indicated transition SOC, as shown in Fig. 6f.

Fig. 6g plots the charge and discharge curves at each stress level, with the SOCs and cell potentials of the phase transitions indicated. Therefore, as phase transitions are shifted to higher SOCs at higher

stress, these transitions happen at higher cell potentials during charge and lower cell potentials during discharge. This is consistent with the shifts in the dQ/dV plots shown in Fig. 1b, where the peaks and troughs are shifted to higher SOCs.

Much of the capacity loss in a constant current charging scheme is due to the voltage shift due to stress (as is discussed in the supplemental document), which can be corrected by adjusting the voltage window of cells under stack pressures. However, the capacity loss due to lithium inventory consumption of phase transitions under stress is less easily fixed. While some systems (such as solid-state batteries) require some stack pressure, if this is not required, high stack pressure should be avoided.

4. Conclusion

We used neutron diffraction on commercial pouch cells to understand how lithium-ion battery electrode materials are affected by an applied stress during charge cycling. We compared single peak fitting results from diffraction patterns of pouch cells charge-cycled at different stresses for the copper current collector, lithium cobalt oxide cathode, and graphite anode phases. It was found that the copper current collector experiences a small strain during charge and discharge due to the expansion of the graphite phases, which is often ignored in these systems. For the graphite and LCO electrodes, the effect of stress on phase transitions was characterized and it was found that phase transitions under higher stresses require more of the available capacity of the battery. These findings are noteworthy for any lithium-ion pouch cell being charged in a constrained space or under stack pressures, including solid-state cells and cells in battery packs, particularly for lithium-ion anodes with larger volume expansion than graphite (such as silicon, tin, aluminum, etc.). The copper current collector should not be assumed to be mechano-electrochemically inactive; in systems with large volume expansions the buildup of internal stresses could potentially lead to mechanical deformation or even failure of the copper. Voltage cutoff windows need to be shifted to account for the loss of capacity due to mechano-electrochemical voltage shifts, and external stresses on pouch cells should be minimized to reduce the capacity loss due to lithium inventory loss during phase transitions under stress.

CRediT authorship contribution statement

Juliane I. Preimesberger: Conceptualization, Formal analysis, Investigation, Visualization, Writing – original draft, Writing – review & editing. **Yan Chen:** Conceptualization, Investigation, Methodology, Supervision, Writing – review & editing. **Ke An:** Conceptualization, Funding acquisition, Project administration, Supervision, Writing – review & editing. **Craig B. Arnold:** Conceptualization, Funding acquisition, Project administration, Resources, Writing – review & editing.

Declaration of competing interest

The authors declare the following financial interests/personal relationships which may be considered as potential competing interests: Juliane I. Preimesberger reports a relationship with National Renewable Energy Laboratory that includes: employment. If there are other authors, they declare that they have no known competing financial interests or personal relationships that could have appeared to influence the work reported in this paper.

Data availability

Data will be made available on request.

Spallation Neutron Source, a DOE Office of Science User Facility operated by the Oak Ridge National Laboratory. The authors thank Dunji Yu and Harley Skorpenske for their support for the neutron experiments.

Appendix A. Supplementary data

Supplementary data to this article can be found online at https://doi.org/10.1016/j.jpowsour.2024.234114.

References

[1] R. Xu, K. Zhao, Electrochemomechanics of electrodes in Li-ion batteries: a review, J. Electrochem. En. Conv. Stor. 13 (2016) 011002, https://doi.org/10.1115/1.4035310.

[2] D.M. Piper, T.A. Yersak, S.-H. Lee, Effect of compressive stress on electrochemical performance of silicon anodes, J. Electrochem. Soc. 160 (2013) A77–A81, https://doi.org/10.1149/2.064301jes.

[3] S.R. Bishop, D. Marrocchelli, C. Chatzichristodoulou, N.H. Perry, M.B. Mogensen, H.L. Tuller, E.D. Wachsman, Chemical expansion: implications for electrochemical energy storage and conversion devices, Annu. Rev. Mater. Res. 44 (2014) 205–239, https://doi.org/10.1146/annurev-matsci-070813-113329.

[4] R. Koerver, W. Zhang, L. de Biasi, S. Schweidler, A.O. Kondrakov, S. Kolling, T. Brezesinski, P. Hartmann, W.G. Zeier, J. Janek, Chemo-mechanical expansion of lithium electrode materials - on the route to mechanically optimized all-solid-state batteries, Energy Environ. Sci. 11 (2018) 2142–2158, https://doi.org/10.1039/C8EE00907D.

[5] J. Cannarella, C.B. Arnold, Stress evolution and capacity fade in constrained lithium-ion pouch cells, J. Power Sources 245 (2014) 745–751, https://doi.org/10.1016/j.jpowsour.2013.06.165.

[6] G. Bucci, T. Swamy, S. Bishop, B.W. Sheldon, Y.-M. Chiang, W.C. Carter, The effect of stress on battery-electrode capacity, J. Electrochem. Soc. 164 (2017) A645–A654, https://doi.org/10.1149/2.0371704jes.

[7] L.D. Sutter, G. Berckmans, M. Marinaro, M. Wohlfahrt-Mehrens, M. Berecibar, J.V. Mierlo, Mechanical behavor of Silicon-Graphite pouch cells under external compressive load: implications and opportunities for battery pack design, J. Power Sources (2020) 451, https://doi.org/10.1016/j.jpowsour.2020.227774.

[8] H. Xie, J. Guo, H. Song, B. Shi, Y. Kang, Active tensile/compressive stress-regulated electrochemical behavior and mechanism in electrodes, Energy Technol. 6 (2018) 1788–1796, https://doi.org/10.1002/ente.201700900.

[9] H. Li, S. Guo, H. Zhou, In-situ/operando characterization techniques in lithium ion batteries and beyond, J. Energy Chem. 59 (2021) 191–211, https://doi.org/10.1016/j.jechem.2020.11.020.

[10] V. Augustyn, R. Wang, N. Balke, M. Pharr, C.B. Arnold, Deformation during electrosorption and insertion-type charge storage: origins, characterization, and design of materials for high power, ACS Energy Lett. 5 (2020) 3548–3559, https://doi.org/10.1021/acsenergylett.0c01823.

[11] D. Liu, Z. Shadike, R. Lin, K. Qian, H. Li, K. Li, S. Wang, Q. Yu, M. Liu, S. Ganapathy, X. Qin, Q.-H. Yang, M. Wagemaker, F. Kang, X.-Q. Yang, B. Li, Review of recent developments of in-situ/operando characterization techniques for lithium battery research, Adv. Mater. 31 (2019) 1806620, https://doi.org/10.1002/adma.201806620.

[12] X. Wang, Y. Sone, G. Segami, H. Naito, C. Yamada, K. Kibe, Understanding volume change in lithium-ion cells during charging and discharging using in situ measurements, J. Electrochem. Soc. 154 (2006) A14–A21, https://doi.org/10.1149/1.2386933.

[13] N. Zhang, H. Tang, Dissecting anode swelling in commercial lithium-ion batteries, J. Power Sources 218 (2012) 52–55, https://doi.org/10.1016/j.jpowsour.2012.06.071.

[14] H. Xie, B. Han, H. Song, X. Li, Y. Kang, Q. Zhang, In-situ measurements of electrochemical stress/strain fields and stress analysis during an electrochemical process, J. Mech. Phys. Solid. 156 (2021) 104602, https://doi.org/10.1016/j.jmps.2021.104602.

[15] J.B. Siegel, A.G. Stefanopoulou, P. Hagans, Y. Ding, D. Gorsich, Expansion of lithium ion pouch cell batteries: observations from neutron imaging, J. Electrochem. Soc. 160 (2013) A1031–A1038, https://doi.org/10.1149/2.011303jes.

[16] E. Zhao, Z.-G. Zhang, X. Li, L. He, X. Yu, H. Li, F. Wang, Neutron-based characterization techniques for lithium battery research, Chin. Phys. B 29 (2020) 018201, https://doi.org/10.1088/1674-1056/ab5d07.

[17] X.L. Wang, K. An, L. Cai, Z. Feng, S.E. Nagler, C. Daniel, K.J. Rhodes, A.D. Stoica, H.D. Skorpenske, C. Liang, W. Zhang, J. Kim, Y. Qi, S.J. Harris, Visualizing the chemistry and structure dynamics in lithium-ion batteries by in-situ neutron diffraction, Sci. Rep. 2 (2012) 747, https://doi.org/10.1038/srep00747.

[18] X. Wu, B. Song, P.-H. Chien, S.M. Everett, K. Zhao, J. Liu, Z. Du, Structural evolution and transition dynamics in lithium ion battery under fast charging: an operando neutron diffraction investigation, Adv. Sci. 8 (2021) 2102318, https://doi.org/10.1002/advs.202102318.

[19] J. Schnell, T. Gunther, T. Knoche, C. Vieider, L. Kohler, A. Just, M. Keller, S. Passerini, G. Reinhart, All-solid-state lithium-ion and lithium metal batteries - paving the way to large-scale production, J. Power Sources 382 (2018) 160–175, https://doi.org/10.1016/j.jpowsour.2018.02.062.

[20] X. Zhang, Q.J. Wang, K.L. Harrison, S.A. Roberts, S.J. Harris, Pressure-Driven interface evolution in solid-state lithium metal batteries, Cell Rep. Phys. Sci. 1 (2020) 100012, https://doi.org/10.1016/j.jpowsour.2018.02.062.

[21] X.L. Wang, T.M. Holden, G.Q. Rennich, A.D. Stoica, P.K. Liaw, H. Choo, C.R. Hubbard, VULCAN-The engineering diffractometer at the SNS, Phys. B Condens. Matter 386 (2006) 673–675, https://doi.org/10.1016/j.physb.2006.06.103.

[22] K. An, H.D. Skorpenske, A.D. Stoica, D. Ma, X.L. Wang, E. Cakmak, First in situ lattice strain measurements under load at VULCAN, Metall. Mater. Trans. 42 (2011) 95–99, https://doi.org/10.1007/s11661-010-0495-9.

[23] C. Didier, W.K. Pang, Z. Guo, S. Schmid, V.K. Peterson, Phase evolution and intermittent disorder in electrochemically lithiated graphite determined using in operando neutron diffraction, Chem. Mater. 32 (2020) 2518–2531, https://doi.org/10.1021/acs.chemmater.9b05145.

[24] N. Douakha, M. Holzapfel, E. Chappel, G. Chouteau, L. Croguennec, A. Ott, B. Ouladdiaf, Nuclear and magnetic structure of layered LiFe(1-x)Co(x)O(2) (0<=x<=1) determined by high-resolution neutron diffraction, J. Solid State Chem. 163 (2002) 406–411, https://doi.org/10.1006/jssc.2001.9413.

[25] B. Vadlamani, K. An, M. Jagannathan, K.S. Ravi Chandran, An in-situ electrochemical cell for neutron diffraction studies of phase transitions in small volume electrodes of Li-ion batteries, J. Electrochem. Soc. 161 (2014) A1731–A1741, https://doi.org/10.1149/2.0951410jes.

[26] S. Kim, S.J. Choi, K. Zhao, H. Yang, G. Gobbi, S. Zhang, J. Li, Electrochemically driven mechanical energy harvesting, Nat. Commun. 7 (2016) 10146, https://doi.org/10.1038/ncomms10146.

[27] N. Muralidharan, M. Li, R.E. Carter, N. Galioto, C.L. Pint, Ultralow frequency electrochemical-mechanical strain energy harvester using 2D black phosphorus nanosheets, ACS Energy Lett. 2 (2017) 1797–1803, https://doi.org/10.1021/acsenergylett.7b00478.

[28] J. Cannarella, C.B. Arnold, Towards low-frequency mechanical energy harvesting using energy-dense piezoelectrochemical materials, Adv. Mater. 27 (2015) 7440–7444, https://doi.org/10.1002/adma.201502974.

[29] J.I. Preimesberger, S. Kang, C.B. Arnold, Figures of merit for piezoelectrochemical energy-harvesting systems, Joule 4 (2020) 1893–1906, https://doi.org/10.1016/j.joule.2020.07.019.

[30] J. Cannarella, C.Z. Leng, C.B. Arnold, On the coupling between stress and voltage in lithium ion pouch cells, Proc. SPIE 9115 (2014) 91150K, https://doi.org/10.1117/12.2055152.

[31] J.I. Preimesberger, S. Kang, Y. Chen, K. An, C.B. Arnold, Investigating mechano-electrochemical coupling phenomenon in lithium ion pouch cells using in-situ neutron diffraction, ECS Trans. 104 (2021) 75–85, https://doi.org/10.1149/10401.0075ecst.

[32] C. Peabody, C.B. Arnold, The role of mechanically induced separator creep in lithium-ion battery capacity fade, J. Power Sources 196 (2011) 8147–8153, https://doi.org/10.1016/j.jpowsour.2011.05.023.

[33] K. An, VDRIVE-data Reduction and Interactive Visualization Software for Event Mode Neutron Diffraction, Oak Ridge National Laboratory, 2012.

[34] R.B. Von Dreele, J.D. Jorgensen, C.G. Windsor, Rietveld refinement with spallation neutron powder diffraction, J. Appl. Crystallogr. 15 (1982) 581–589, https://doi.org/10.1107/S0021889882012722.

[35] J.N. Reimers, J. Dahn, Electrochemical and in situ X-ray diffraction studies of lithium intercalation in Li x CoO2, J. Electrochem. Soc. 139 (1992) 2091–2097, https://doi.org/10.1149/1.2221184.

[36] N. Takami, A. Satoh, M. Hara, T. Ohsaki, Structural and kinetic characterization of lithium intercalation into carbon anodes for secondary lithium batteries, J. Electrochem. Soc. 142 (1995) 371–379, https://doi.org/10.1149/1.2044017.

[37] Z. Schiffer, J. Cannarella, C.B. Arnold, Strain derivatives for practical charge rate characterization of lithium ion electrodes, J. Electrochem. Soc. 163 (2016) A427–A433, https://doi.org/10.1149/2.0091603jes.

[38] L. Cai, K. An, Z. Feng, C. Liang, S.J. Harris, In-situ observation of inhomogeneous degradation in large format Li-ion cells be neutron diffraction, J. Power Sources 236 (2013) 163–168, https://doi.org/10.1016/j.jpowsour.2013.02.066.

[39] M.T. Hutchings, P.J. Withers, T.M. Holden, T. Lorentzen, Introduction to the Characterization of Residual Stress by Neutron Diffraction, CRC Press, 2005.

[40] Y. Chen, I. Cernatescu, V. Venkatesh, A.D. Stoica, K. An, On the residual stress relaxation in Inconel 718 superalloys at high temperature by real-time neutron diffraction, Mater. Des. 232 (2023) 112135, https://doi.org/10.1016/j.matdes.2023.112135.

[41] D. Li, H. Liu, H. Wan, Y. Wang, J. Zhang, Effect of state-of-charge and air exposure on tensile mechanical properties of lithium-ion battery electrodes, J. Energy Storage 56 (2022) 106018, https://doi.org/10.1149/1945-7111/ab8804.

[42] X. Yu, Z. Feng, Y. Ren, D. Henn, Z. Wu, K. An, B. Wu, C. Fau, C. Li, S.J. Harris, Simultaneous operando measurements of the local temperature, state of charge, and strain inside a commercial lithium-ion pouch cell, J. Electrochem. Soc. 165 (2018) A1578–A1585. https://iopscience.iop.org/article/10.1149/2.1251807jes/meta.

[43] Z. Pan, T. Sedlatschek, Y. Xia, Real time characterization of the current collector's role on the electro-chemo-mechanical coupling performance of Si composite electrode, J. Electrochem. Soc. 167 (2020) 090517, https://doi.org/10.1021/acsenergylett.0c01823.

[44] A. Senyshyn, V. Baran, M.J. Mühlbauer, M. Etter, M. Schulz, K. Tu, Y. Yang, Uniformity of flat Li-ion batteries studied by diffraction and imaging of X-rays and neutrons, ACS Appl. Energy Mater. 4 (2021) 3110–3117. https://pubs.acs.org/doi/full/10.1021/acsaem.0c02844.